

www.acsami.org Research Article

Influence of Halides on the Interactions of Ammonium Acids with Metal Halide Perovskites

Yanan Li, Patrick J. Lohr, Allison Segapeli, Juliana Baltram, Dorian Werner, Alex Allred, Krishna Muralidharan, and Adam D. Printz*



Cite This: https://doi.org/10.1021/acsami.3c01432



ACCESS I

III Metrics & More

Article Recommendations

Supporting Information

ABSTRACT: Additive engineering is a common strategy to improve the performance and stability of metal halide perovskite through the modulation of crystallization kinetics and passivation of surface defects. However, much of this work has lacked a systematic approach necessary to understand how the functionality and molecular structure of the additives influence perovskite performance and stability. This paper describes the inclusion of low concentrations of 5-aminovaleric acid (5-AVA) and its ammonium acid derivatives, 5-ammoniumvaleric acid iodide (5-AVAI) and 5-ammoniumvaleric acid chloride (5-AVACl), into the precursor inks for methylammonium lead triiodide (MAPbI₃) perovskite and highlights the important role of halides in affecting the interactions



of additives with perovskite and film properties. The film quality, as determined by X-ray diffraction (XRD) and photoluminescence (PL) spectrophotometry, is shown to improve with the inclusion of all additives, but an increase in annealing time from 5 to 30 min is necessary. We observe an increase in grain size and a decrease in film roughness with the incorporation of 5-AVAI and 5-AVACI with scanning electron microscopy (SEM) and atomic force microscopy (AFM). Critically, X-ray photoelectron spectroscopy (XPS) measurements and density functional theory (DFT) calculations show that 5-AVAI and 5-AVACI preferentially interact with MAPbI₃ surfaces via the ammonium functional group, while 5-AVA will interact with either amino or carboxylic acid functional groups. Charge localization analysis shows the surprising result that HCI dissociates from 5-AVACI in vacuum, resulting in the decomposition of the ammonium acid to 5-AVA. We show that device repeatability is improved with the inclusion of all additives and that 5-AVACI increases the power conversion efficiency of devices from 17.61 \pm 1.07 to 18.07 \pm 0.42%. Finally, we show stability improvements for unencapsulated devices exposed to 50% relative humidity, with devices incorporating 5-AVAI and 5-AVACI exhibiting the greatest improvements.

KEYWORDS: hybrid organic-inorganic lead halide perovskites, perovskite solar cells, ammonium halide salt additives, multifunctional additives, surface passivation, halide exchange, first principles

1. INTRODUCTION

Metal halide perovskites, or simply "perovskites," are promising materials for next-generation photovoltaic applications due to their excellent optoelectronic properties, such as direct and tunable band gaps, long carrier-diffusion lengths, high charge-carrier mobilities, and high absorption coefficients. These properties have resulted in perovskite-based solar cells (PSCs) achieving power conversion efficiencies (PCEs) on par with more mature technologies such as crystalline silicon in just over a decade. However, poor chemical and thermomechanical stabilities remain an obstacle that must be addressed for these promising technologies to ever achieve commercial viability. A,8-10

Additive engineering is commonly used in metal halide perovskite-based materials to address instabilities, predominantly through two mechanisms: (1) controlling crystallization kinetics and (2) passivating surface defects.^{4,11} The two

pathways for additive engineering are to add the additives either directly into the precursor ink or after film formation in a postprocessing step. When the additives are added directly into the perovskite precursor solution, they will interact with the perovskite precursors, forming adducts that regulate the perovskite crystallization, which can lead to improved film quality. If these additives are not volatilized during film growth, they can passivate surface defects by interacting with the perovskite grain surfaces through coordination bonding—e.g., Lewis acid/base interactions. 12-15 While the general

Received: January 31, 2023 Accepted: April 26, 2023



strategy of additive engineering has been shown to be highly effective, there are still many remaining questions about how additives interact with perovskite precursors and films on the molecular level. These questions must be answered to understand how to best implement this strategy—i.e., selecting the most appropriate additives for a given material composition and application—especially as the field moves toward increasingly complex metal halide perovskites that incorporate mixed cations, metals, and halides.

One particularly common class of additives that have frequently been shown to improve material properties are additives with amino and ammonium functional groups. 12,14,16 These additives typically interact with the perovskite through Lewis acid-base interactions between the amines and the soft Lewis acid Pb²⁺ or through the hydrogen bonding between the hydrogens on ammonium and halide species on the surface of perovskite grains to improve chemical stability by reducing surface reactivity. 12,14,17 One exemplary family of these additives is 5-aminovaleric acid (5-AVA) and its ammonium/ halide salts 5-AVAX (X = I, Cl, or Br). These bifunctional additives include amino (or ammonium) and carboxyl groups, which enable the passivation of multiple defect types and linking of adjacent grains via Lewis acid-base coordination and hydrogen-bonding interactions, thus improving the stability and performance of perovskites. In 2014, Mei et al. first added 5-AVAI as an additive into methylammonium lead triiodide (MAPbI₃) perovskite precursor solution and built mesoscopic perovskite solar cells with a certified PCE of 12.8% and stability >1000 h in ambient air under full sunlight. 18 The enhanced PCE and stability were attributed to the templating role of 5-AVAI in perovskite crystal nucleation and vertical growth, where carboxyl groups anchored to mesoporous TiO2 and ZrO2 substrate, and amino groups promoted nucleation and filled the pores. Later, Grancini et al. reported a twodimensional/three-dimensional (2D/3D) (5-AVA)₂PbI₄/ MAPbI₃ perovskite and realized an outstanding long-term stability over one year (>10,000 h) without any loss in PCE.¹⁹ More recently, 5-AVAI was also shown to produce better stability and higher PCEs in formamidinium (FA)-based²⁰ and Sn-based perovskite.²¹ Furthermore, both 5-AVAI and 5-AVA have also been demonstrated to improve the mechanical properties—i.e., the cohesive energies—of MAPbI₃.8,13

Although there are a significant number of reports demonstrating the incorporation of 5-AVA^{8,13,22,23} or 5-AVAI into metal halide perovskites to enhance efficiency or mechanical stability, ^{18,20,21,24,25} 5-AVACI has been rarely used as an additive, despite previous demonstrations of chloride (Cl⁻) alloying significantly improving the quality of perovskite by increasing grain size and reducing the number of trap states. ^{26–31} Furthermore, despite the significant body of literature, a detailed understanding of how the 5-AVA/5-AVAX family of additives interacts with perovskite precursors or grain surfaces is still lacking, and in particular, there is a dearth of studies that have explicitly focused on the effect of the halides in this additive family. In many cases, the identity of the halide species is omitted and both the amino and protonated ammonium acid forms of 5-aminovaleric acid are referred to as 5-AVA.

In this work, we aimed to understand how the modification of amino/ammonium halide functionality influenced the performance and stability of perovskite films and devices by comparing a series of amino/ammonium additives with changes to the halide composition. We therefore wanted to

compare the influence of the halide counterions, iodide and chloride, on the perovskite films. To avoid confusion, we will refer to 5-aminovaleric acid as 5-AVA and the ammonium acid forms as 5-AVAX as a generalized form, or 5-AVAI and 5-AVACI for 5-ammoniumvaleric acid iodide and 5-ammoniumvaleric acid chloride, respectively.

To reduce the complexity of the system to better isolate the effects of the halides in the additives, we focused on MAPbI₃ perovskite given its simpler chemistry than mixed cation/anion perovskites. We introduced 5-AVA and two of its halide salts, 5-AVAI and 5-AVACl, into MAPbI₃ perovskite precursor solutions to study their interaction with perovskite through experiment and density functional theory (DFT) calculations. Our results showed that the halides played different roles in the properties of MAPbI₃ films. At concentrations of 1 mol % 5-AVA/5-AVAX relative to Pb²⁺, generally beneficial effects were observed. At higher concentrations—5 or 10 mol %—5-AVA and 5-AVAX were detrimental to PCE. Moreover, we observed stronger interaction energies between perovskites and the 5-AVAX ammonium/halide salts than with the 5-AVA amino acid, which resulted in slower crystallization and larger grain size. As a result, devices incorporating 5-AVAI and 5-AVACI exhibited the highest stability and reproducibility. The addition of 5-AVACl also significantly reduced nonradiative recombination, as evidenced by photoluminescence measurements, and enhanced the average PCE from 17.61 \pm 1.07 to 18.07 \pm

2. EXPERIMENTAL METHODS

2.1. Materials. Indium tin oxide (ITO)-coated glass slides ($R_s \sim$ 10 Ω □⁻¹) were purchased from Xin Yan Technology. Lead(II) acetate trihydrate (PbAc2·3H2O, 99.999%) and anhydrous N,Ndimethylformamide (DMF, 99.8%) were purchased from Sigma-Aldrich. Methylammonium iodide (MAI) was purchased from GreatCell Solar Materials. 5-Aminovaleric acid (5-AVA, 98%), 5ammoniumvaleric acid chloride (5-AVACl, 98%), and 5-ammoniumvaleric acid iodide (5-AVAI, 97%) were purchased from TCI Chemicals. Tin(IV) oxide (SnO₂, 15% in H₂O colloidal dispersion), lithium bis(trifluoromethylsulfonyl)imide (LiTFSI, 98%), and anhydrous toluene (99.8%) were purchased from Alfa Aesar. 4-tert-Butylpyridine (tBP, 96%) was purchased from Shanghai Shaoyuan Co., Ltd. Poly[bis(4-phenyl)(2,4,6-trimethylphenyl)amine] (PTAA, Mw: 40 kDa) was purchased from Solaris Chem. 2-Propanol (certified ACS) and acetone (certified ACS) were purchased from Fischer Scientific. All chemicals were used as received without further purification.

2.2. Preparation of Samples for XRD, PL, UV–Vis, SEM, AFM, and XPS. Microscope glass substrates $(1 \times 1 \text{ in.})$ were sequentially cleaned by ultrasonication in 1 wt % Alconox detergent solution, deionized water, acetone, and isopropanol for 10 min each and then exposed to oxygen plasma at 120 W for 5 min. The MAPbI₃ perovskite precursor solution was prepared in a N₂-filled glovebox by dissolving 341.4 mg mL⁻¹ PbAc₂ and 429.3 mg mL⁻¹ MAI in anhydrous DMF with continuous stirring on a 70 °C hotplate for 1 h, forming a 0.9 M (with respect to Pb²⁺) perovskite solution.

After cooling to room temperature, the perovskite solution was filtered with a 0.2 μm poly(tetrafluoroethylene) (PTFE) filter and then spin-coated onto the glass substrate at 2000 rpm (2000 rpm s $^{-1}$ ramp rate) for 75 s (after 15 s, N $_2$ was flowed at 20 psi into the spin coater to improve film morphology). The wet films were then annealed at 100 °C for 2–30 min. For films fabricated from inks with additives, different amounts of 5-AVA, 5-AVACl, or 5-AVAI (1–10 mol % with respect to Pb $^{2+}$) were directly mixed with the precursor solution and the films were prepared following the same procedure described above. These films were used for XRD, PL, ultravioletvisible (UV–vis), SEM, and AFM characterization.

ACS Applied Materials & Interfaces

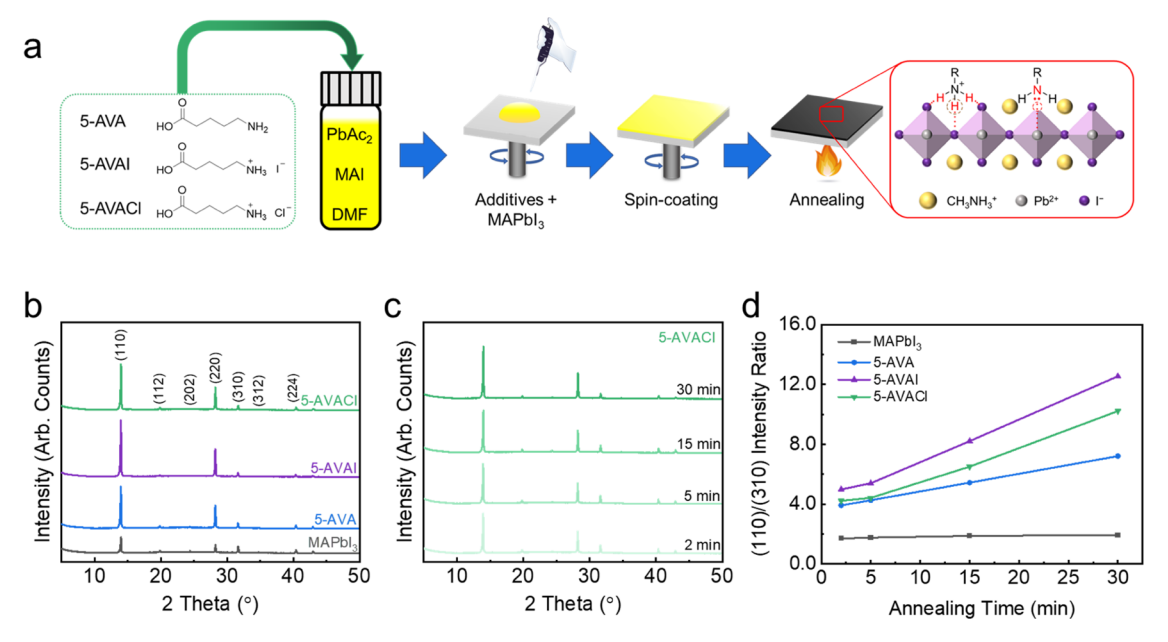


Figure 1. (a) Chemical structures of 5-AVA, 5-AVAI, and 5-AVACl and fabrication process schematic. (b) XRD spectra of the pristine MAPbI $_3$ film and the films incorporated with 1 mol % 5-AVAI, and 5-AVACl after 30 min of annealing at 100 °C. (c) XRD spectra of 1 mol % 5-AVACl-modified films at different annealing times. (d) (110)/(310) intensity ratio in MAPbI $_3$ films with and without additives as a function of annealing time.

Films for XPS were prepared differently; pristine perovskite films were coated with a 0.01 mmol $\rm ml^{-1}$ 5-AVA, 5-AVACl, or 5-AVAI solution in IPA by spin-coating at 2000 rpm for 30 s and then annealed at 100 °C for 5 min.

2.3. X-ray Diffraction Measurements. The crystal structure of the perovskite films was characterized by powder XRD measurements, using a Phillips X'Pert Pro MPD X-ray diffractometer with Cu $K\alpha$ radiation (λ = 1.54 Å). XRD spectra were collected from 5 to 50° with a step size of 0.017° and a scan speed of 0.209° s⁻¹.

2.4. Photoluminescence and UV–Vis Absorption Spectroscopy. Steady-state photoluminescence spectra were measured at room temperature using a Horiba Fluorolog-3 Spectrofluorometer equipped with a 450 W xenon lamp. The perovskite films were excited with the 430 nm line of the Xenon lamp. Time-resolved photoluminescence (TRPL) was performed using a DeltaHub time-correlated single photon counting (TCSPC) module with a NanoLED pulsed diode laser source at 639 nm (Horiba NanoLED DD-635L, 60 ps pulse duration) and a repetition rate of 20 MHz.

UV—vis absorption spectra of the sample films were collected using a Cary 5000 UV—vis-NIR spectrophotometer in the range of 400— 850 nm with 1 nm intervals. A blank glass substrate was used as the reference slide for baseline correction.

2.5. Scanning Electron Microscopy and Grain Size Measurements. The morphology and grain sizes of the perovskite films were characterized by a Hitachi S-4800 SEM, operated at 10.0 kV and 10 μ A. Samples were coated with 5 nm of Pt prior to microscopy to improve conductivity and minimize image distortion by charging effects.

The obtained micrographs with magnifications of $25,000\times$ and $50,000\times$ were processed, and the grain sizes were estimated using ImageJ. In ImageJ, the grains were manually outlined using the polygon selection tool to build the grain boundary map. The grain sizes were then calculated by running the "Analyze \rightarrow measure" routine in ImageJ. For each film composition, at least 100 grains were analyzed.

2.6. Atomic Force Microscopy. Surface morphology and roughness characterization of the perovskite films were conducted on a Park NX20 AFM using Al-coated silicon cantilevers (HQ:NSC15/Al BS) with the frequency of 325 kHz, a force constant of 40 N m⁻¹, 125 μ m length, 30 μ m width, and operating under noncontact mode.

2.7. X-ray Photoelectron Spectroscopy Measurements. XPS spectra were acquired on a Kratos Axis Ultra Photoelectron Spectrometer with a monochromated Al $K\alpha$ radiation (1486.6 eV), operated at 15 kV/20 mA and pass energy of 20 eV.

2.8. Modeling Intermolecular Interactions. Adsorption calculations were performed using the Perdew-Burke-Ernzerhof (PBE) generalized gradient approximation (GGA) with Grimme's DFT-D3 dispersion correction as implemented in the Vienna Ab initio Simulation Package (VASP). 32-37 Valence-core interactions were treated with the projector augmented wave (PAW) method, and the energy cutoff for plane waves was 520 eV. All structures were fully relaxed using a conjugate-gradient algorithm until the force on each constituent atom was less than 0.01 eV Å⁻¹. A Γ -centered 4 \times 4 \times 1 and $8 \times 8 \times 8$ Monkhorst-Pack k-point mesh was used for all slab calculations and unit cells, respectively.³⁸ MA-I- and Pb-I-rich surfaces were prepared by cleaving supercells of pseudocubic perovskite along the (001) direction and introducing 25 Å of vacuum in the direction normal to the slab surface. The optimal cleaved surface area for adsorption was determined by increasing the supercell size until calculated energies were converged for all 5-AVAX species. For all of the calculations, the bottom layer of unit cells was fixed and the number of mobile layers was varied to ensure the convergence of relative adsorption energies. Dipole corrections were applied in the direction normal to the slab surface corresponding to IDIPOL = 3 in VASP.

When DFT calculations were performed on isolated molecules for subsequent adsorption calculations with VASP, geometrically optimized energies were produced by placing each adsorbate in the center of a cubic simulation cell of side length 30 Å. A Γ -centered 1 \times 1 \times 1 Monkhorst–Pack k-point mesh was used for Brillouin zone integration, and dipole corrections were applied in all Cartesian directions. All atomistic visualization was performed with the Visualization for Electronic and Structural Analysis (VESTA) software package. 39

Electrostatic potential maps for 5-AVA/5-AVAX were calculated using the Gaussian 16 software package. All molecular configurations were relaxed using the ω B97X-D range-corrected hybrid functional at the def2-TZVP level of theory, ^{40,41} and frequency analysis was performed to check for the presence of saddle points during optimization.

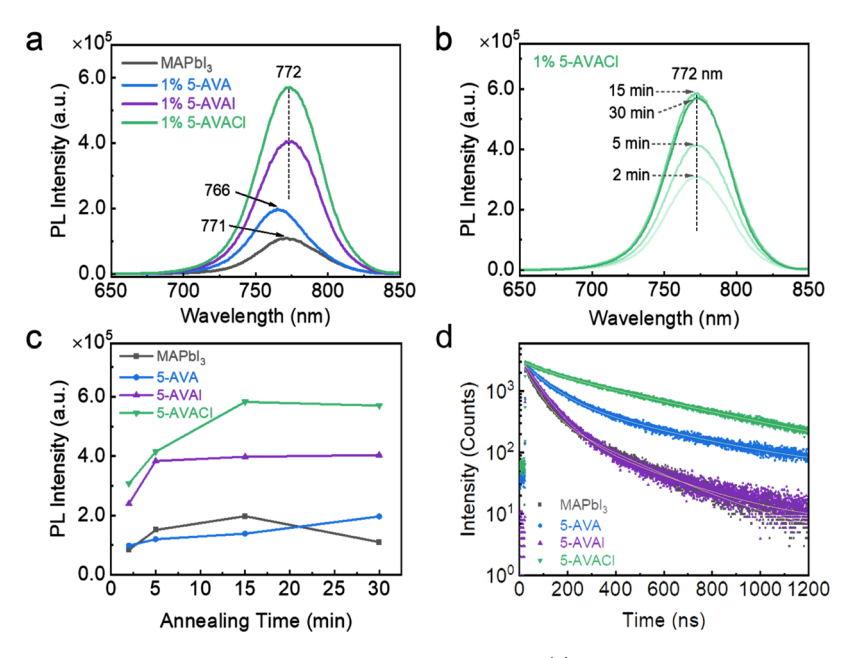


Figure 2. Photoluminescence properties of MAPbI₃ films with and without additives. (a) Steady-state PL of films of pristine MAPbI₃ and MAPbI₃ incorporating 1 mol % 5-AVA, 5-AVAI, and 5-AVACl. (b) PL spectra of MAPbI₃ with 1 mol % 5-AVACl at different annealing times. (c) PL intensity of MAPbI₃ films with and without additives as a function of annealing time. (d) Time-resolved PL of MAPbI₃ films with and without additives.

2.9. Preparation and Characterization of Solar Cells. ITOcoated glass substrates (2 cm × 2 cm) were cleaned as described in Section 2.2. A diluted 4 wt % of SnO₂ solution was spin-coated on ITO substrate at 4000 rpm (4000 rpm s⁻¹ ramp rate) for 30 s and annealed at 150 °C for 1 h, resulting in a 30 nm thick SnO₂ film. The perovskite ink (with/without additives) was spin-coated onto the SnO₂ layer following the same procedure described in Section 2.2. Subsequently, 15 mg mL⁻¹ of PTAA in anhydrous toluene, doped with $10~\mu L~mL^{-1}$ of LiTFSI solution (170 mg mL⁻¹) and $6~\mu L~mL^{-1}$ of tBP, was spin-coated on top of the perovskite layer at 4000 rpm (2000 rpm s⁻¹ ramp rate) for 45 s and annealed at 75 °C for 5 min, resulting in a 30 nm thick doped PTAA film. Next, the devices were placed in a desiccator and oxidized overnight to improve hole transport in the PTAA layer. Finally, 150 nm of Ag was e-beam evaporated on top of the devices through a shadow mask, giving a PSC device with the structure ITO/SnO₂/MAPbI₃/PTAA/Ag with an active area of 0.12 cm².

Devices were characterized by current density–voltage (J-V) curves measured using a Keithley 2400 source meter with a scan rate of 0.02 s per step (0.01 V) under simulated solar illumination (AM 1.5G, 100 mW cm⁻²) generated by OAI TriSol TSS-100US AAA solar simulator, which was calibrated by a silicon reference cell.

3. RESULTS AND DISCUSSION

3.1. Characterization of Perovskite Crystallinity. Amino/ammonium acid additives are commonly reported surface or interfacial passivators, typically incorporated into the films by a second step of processing where they are spin-coated onto the surface of a perovskite film. ^{19,25} In this study, we focused on incorporating amino/ammonium acid additives—5-AVA, 5-AVAI, and 5-AVACl with varying concentrations (from 1 to 10 mol % relative to Pb)—directly into the precursor solution since single-step processing is more directly

We evaluated the quality of the perovskite in both pristine and additive-incorporated films using X-ray diffraction (XRD) (Figure 1b). The largest diffraction peaks for the pristine (control) MAPbI₃ sample were at $2\theta = 14.0$, 28.2, and 31.6° , which corresponded to the (110), (220), and (310) crystal

translatable to scalable fabrication (Figure 1a).

planes of a typical tetragonal structure of 3D MAPbI₃. 42 The peaks were at identical locations for all films with 1 mol % 5-AVA/5-AVAX, indicating that the crystal structure was not affected by the inclusion of additives at low concentrations. Moreover, at similar film thicknesses, the intensity of the (110) peak in films incorporating 5-AVA/5-AVAX was approximately twice as high as for the pristine film (Table S1), suggesting that the additives slowed down crystallization and improved the long-range order of the perovskite films. 14,21,28,43 We studied the structural evolution of perovskite films by varying the annealing time and tracking the increased intensity of the (110) peaks for all samples over 30 min of annealing (Figures 1c, S2, and S3). In pristine MAPbI₃ films, the crystallization process was nearly completed within 5 min and there was only a slight increase of the (110) peak intensity in the subsequent samples after 15 and 30 min of annealing (Figures S2 and S3, and Table S1). Conversely, in the films incorporating 5-AVA/ 5-AVAX additives, a notable monotonic increase in (110) peak intensity was observed throughout the 30 min of the annealing process (Figure 1c and Table S1). This increase in (110) peak intensity indicated a continuing improvement of perovskite crystallinity with longer annealing times, which could again be explained by the slowing of perovskite crystallization and templated growth by the incorporation of the additives. 18 Similar increases in (110) peak intensity as a function of annealing time were also observed in 5 and 10 mol % additives samples (Figure S3), although the (110) intensity dropped after the 30 min of annealing for the 10 mol % 5-AVACl sample, which was attributed to the partial conversion of threedimensional perovskite to two-dimensional slabs (Figure S1b). Furthermore, the full width at half-maximum (FWHM) of (110) peaks narrowed with the inclusion of additives as well as increased annealing times (Table S2).

Previous reports have used the ratio of the intensities of the (110) and (310) peaks to indicate the extent of crystal orientation; 44,45 in our films, the additive-modified films showed much higher (110)/(310) intensity ratios—7.21,

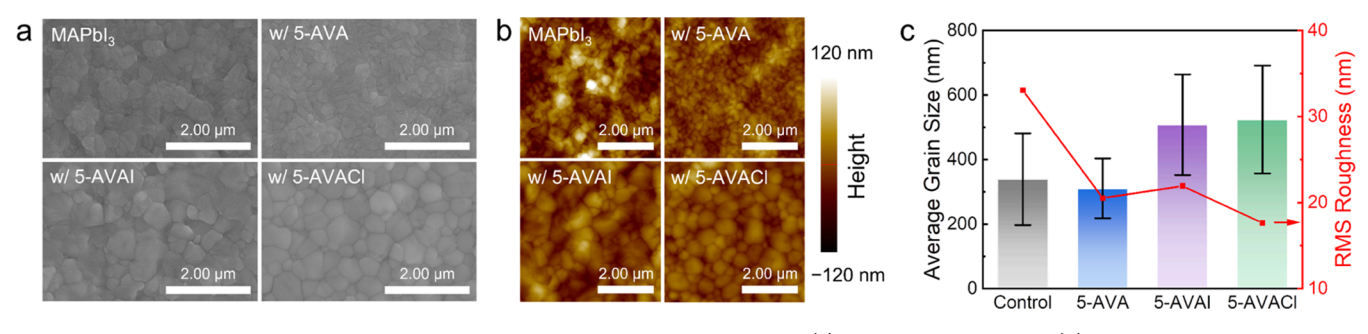


Figure 3. Morphologies of MAPbI₃ films with and without 5-AVA/5-AVAX additives. (a) SEM micrographs and (b) AFM micrographs of pristine MAPbI₃ and MAPbI₃ with 1 mol % of 5-AVA, 5-AVAI, and 5-AVACl after 30 min of annealing, and (c) their average grain size and surface roughness.

12.55, and 10.22 with the inclusion of 5-AVA, 5-AVAI, and 5-AVACl, respectively—than the pristine MAPbI₃ (1.94), consistent with enhanced preferential crystal orientation along the (110) plane induced by the inclusion of 5-AVA/5-AVAX additives (Figure 1d). Notably, the films incorporating 5-AVAI and 5-AVACl exhibited higher (110)/(310) ratios than films incorporating 5-AVA, which we attributed to the additional benefits from the hydrogen bonding between ammonium groups and iodide in the perovskite.

Similarly, at higher concentrations of additives, we observed that the crystallinity and crystal orientation were further enhanced (Figures S1 and S3). Furthermore, at concentrations of 10 mol %, the emergence of a new small diffraction peak at $2\theta = 5.7^{\circ}$ was observed in films with 5-AVA and 5-AVACl (Figure S1b), indicative of 2D perovskite formation according to previous theoretical and experimental reports of 5-AVAX incorporation. Interestingly, this peak was not visible in the 5-AVAI films, suggesting that the 5-AVAI does not form 2D perovskite as readily.

3.2. Characterization of Perovskite Optical Properties. We measured both the steady-state and time-resolved photoluminescence (PL) properties of the perovskite and perovskite/additive films on glass to better understand the influence of 5-AVA/5-AVAX on defect passivation. Given that the additives were expected to passivate surface defects and influence the extent of radiative and deleterious nonradiative recombination of excited electrons and holes, we expected pronounced changes in the photoluminescence characteristics of these films.

The steady-state measurements were performed with an excitation wavelength of 430 nm, which allowed us to probe photoemission from 3D perovskite, which occurs around 760-780 nm, as well as any 2D perovskite that may have formed, which has lower emission wavelengths ranging from 500 to 600 nm. 48 Compared to pristine MAPbI₃, all additives resulted in increased PL intensity, which was consistent with a passivation of surface defects that result in nonradiative recombination. The inclusion of just 1 mol % 5-AVA doubled the PL intensity, while the inclusion of 5-AVAI resulted in a 4-fold increase in intensity and 5-AVACl increased the intensity nearly 6-fold (Figure 2a). The location of the maximum intensity peaks for films with 5-AVAX species was essentially identical to the pristine control, while the inclusion of 5-AVA did result in a slight blue shift (0.0105 eV), which we attributed to the smaller grain size and poorer crystalline quality of films containing 5-AVA. 49 The FWHM was 48.93 nm for the control film, and 44.84, 49.85, and 50.25 nm for the films with 5-AVA, 5-AVAI, and 5-AVACl, respectively. The reduction in FWHM

for the films with 1 mol % 5-AVA might be related to a narrower grain size distribution. 50

We also observed that the PL emission evolved with prolonged annealing time (Figures 2b,c, and S4a-c). In pristine MAPbI₃ films, the PL intensity increased for the first 15 min of annealing and then decreased after 30 min of annealing, possibly due to the thermal decomposition of the perovskite. 51 Films incorporating additives either continued to exhibit increased PL intensity after 30 min of annealing (5-AVA) or stabilized after 15 min of annealing (5-AVAI and 5-AVACl). These longer annealing times were likely necessary for films incorporating additives due to slower crystallization kinetics. At higher concentrations of additives, the maximum PL emission peaks blue-shifted slightly with increasing additive concentration (Figure S4d-f), which was attributed to better passivation of surface defects.⁵² Moreover, at a concentration of 10 mol %, we observed some PL emission at 500-600 nm wavelength in the films with 5-AVA and 5-AVACl (Figure S4f), confirming the low-dimensional perovskite formation observed with XRD as discussed above, 48 while no 2D perovskite emission was detected in films with 5-AVAI.

We then measured the time-resolved photoluminescence of these films with an excitation wavelength of 639 nm (Figure 2d) and used a biexponential fit to determine the photoluminescence lifetimes (Table S3). All films with additives had improved lifetimes compared to the pristine MAPbI3, although the pristine MAPbI3 films and those with 5-AVAI had very similar τ_2 lifetimes of 239.14 and 267.18 ns, respectively. Adding 5-AVA increased the lifetime to 414.43 ns and an even larger lifetime improvement to 493.53 ns was observed with the inclusion of 5-AVACl. The similarity in photoluminescence lifetimes between pristine MAPbI₃ and films containing 5-AVAI was unexpected. Previous reports suggest that these lifetime similarities could be attributable to the formation of iodide interstitial and Frenkel defects near the surface of perovskite grains, which can facilitate the self-trapping of polarons on Pb-I-rich surfaces that would likely occur with the additional iodine provided to the perovskite by the 5-AVAI.⁵³ In the case of 5-AVACl, the addition of the more electronegative chloride species likely localized to the deleterious defects at grain boundaries, where it has been demonstrated to destabilize trapped polarons that lead to fast nonradiative combination.5

Similar absorbance spectra were measured for all thin-film samples in the wavelength range of 400–850 nm, with the band-edge absorption around 780 nm. We estimated the optical band gaps of all films using Tauc plots and found that they were relatively invariant, ranging from 1.594 eV for the

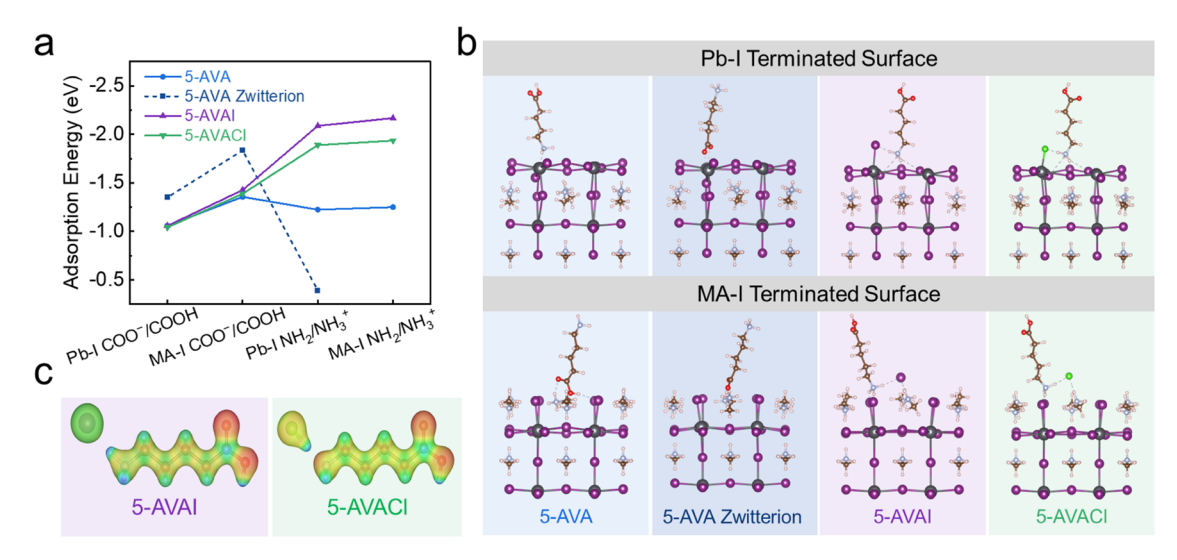


Figure 4. Simulated interactions of the perovskite and additives. (a) DFT-calculated adsorption energies for amino/ammonium and carboxyl functional groups on methylammonium iodide-rich (MA-I) and lead iodide-rich (Pb-I) surfaces. (b) Most energetically favorable adsorption geometries for nonzwitterionic 5-AVA, zwitterionic 5-AVA, 5-AVAI, and 5-AVACl on Pb-I (top row) and MA-I (bottom row) terminated surfaces. (c) Electrostatic potential maps for 5-AVAI and 5-AVACl.

pristine MAPbI₃ to 1.597 eV for the perovskite with 5-AVA (Figure S5). These band gaps were in the typical range for MAPbI₃, ⁵⁶ with the slightly larger bandgap of films incorporating the additives possibly attributable to charge transfer between the additives and perovskite surface shifting trap states and band edges. ¹⁶

3.3. Characterization of Perovskite Morphology. We characterized the perovskite film surfaces with scanning electron microscopy (SEM) and atomic force microscopy (AFM) (Figure 3a,b). We used SEM micrographs to calculate the grain sizes with ImageJ (Figure S6). All films were polycrystalline with varying grain sizes; the average grain size in the pristine films was 339.38 \pm 142.43 nm, while the addition of 5-AVA resulted in a decreased average grain size to 310.89 ± 92.79 nm (Figures 3c and S7), but with a more uniform distribution. We attributed the decrease in grain size with the addition of the 5-AVA to the presence of the amino groups acting as nucleation sites, leading to more small crystallites, in agreement with previous work by Durrant, McLachlan, and coworkers.⁵⁷ Conversely, films incorporating 5-AVAI and 5-AVACl exhibited markedly larger grain sizes of 508.00 \pm 153.91 and 524.55 \pm 167.15 nm (Figures 3b and S7), indicating that these additives effectively improved the morphology of the perovskite through the mediation of crystallization kinetics and possibly templated growth.

Moreover, AFM measurements showed a decrease in surface roughness from 33.06 nm in the pristine perovskite to 20.53, 21.93, and 17.62 nm for the films with 5-AVA, 5-AVAI, and 5-AVACI, respectively (Figure 3b). When comparing the effects of 5-AVAX additives, the slightly larger grain size and lower surface roughness observed in films with 5-AVACI were attributed to slower crystallization kinetics due to a multistep process to form MAPbI₃. Li et al. previously suggested that the perovskite precursors will preferentially interact with Cl⁻ over I⁻ due to the smaller ionic radius and greater electronegativity of Cl⁻, forming MAPbCl₃ first before converting to MAPbI₃.

3.4. Characterization of the Interaction between Perovskite Surfaces and Additives. We performed a series of DFT adsorption calculations and XPS experiments to determine how incorporated additives interact with the

MAPbI₃ surfaces. Adsorption calculations revealed the preferential adsorption energy for each functional group in 5-AVA/5-AVAX, while XPS confirmed these predictions. Previous studies on the incorporation of chloride or bromide ions into MAPbI₃ perovskite have demonstrated that incorporating these halide species into pristine grains is energetically unfavorable, suggesting that halide exchange may occur during the thermal annealing process.^{30,54} Building upon this observation, we hypothesized that the halide species X⁻ would remain electrostatically bound to the positively charged 5-AVA⁺ cation and remain free to passivate any undercoordinated lead species on the surface of the perovskite grains.

We characterized the molecular interactions between 5-AVA/5-AVAX and perovskite surfaces with first-principles calculations using Kohn-Sham density functional theory (DFT). Starting with a pristine $2 \times 2 \times 2$ supercell of pseudocubic MAPbI₃ perovskite, methylammonium iodiderich, and lead iodide-rich surfaces were prepared by cleaving along the (001) direction at different planes. Next, 5-AVA, 5-AVAI, and 5-AVACl were adsorbed to these surfaces, allowing only one functional group to interact with the perovskite surface at a time to determine the relative strength of interaction. Additionally, we performed adsorption calculations with 5-AVA in its zwitterionic state, as this conformation is possible, despite the excess of MAI present in the perovskite precursor solutions. While it has been reported that the preferred surface termination is MA-I rich in pristine MAPbI₃ perovskites, the presence of additives which form adducts in the precursor solution could potentially kinetically trap different surface terminations, so we explored both MA-Iand Pb-I-rich surface terminations. 58,59 We defined the adsorption strength of the additives on both the MA-I- and Pb-I-rich (001) surfaces of MAPbI₃ perovskite by eq 1

$$E_{\rm ads} = E_{\rm slab+additive} - (E_{\rm slab} + E_{\rm additive})$$
 (1)

where $E_{\rm ads}$ is the adsorption energy of the additives to the surface, $E_{\rm slab+additive}$ is the energy corresponding to the optimized adsorption geometry in vacuum, $E_{\rm slab}$ is the energy

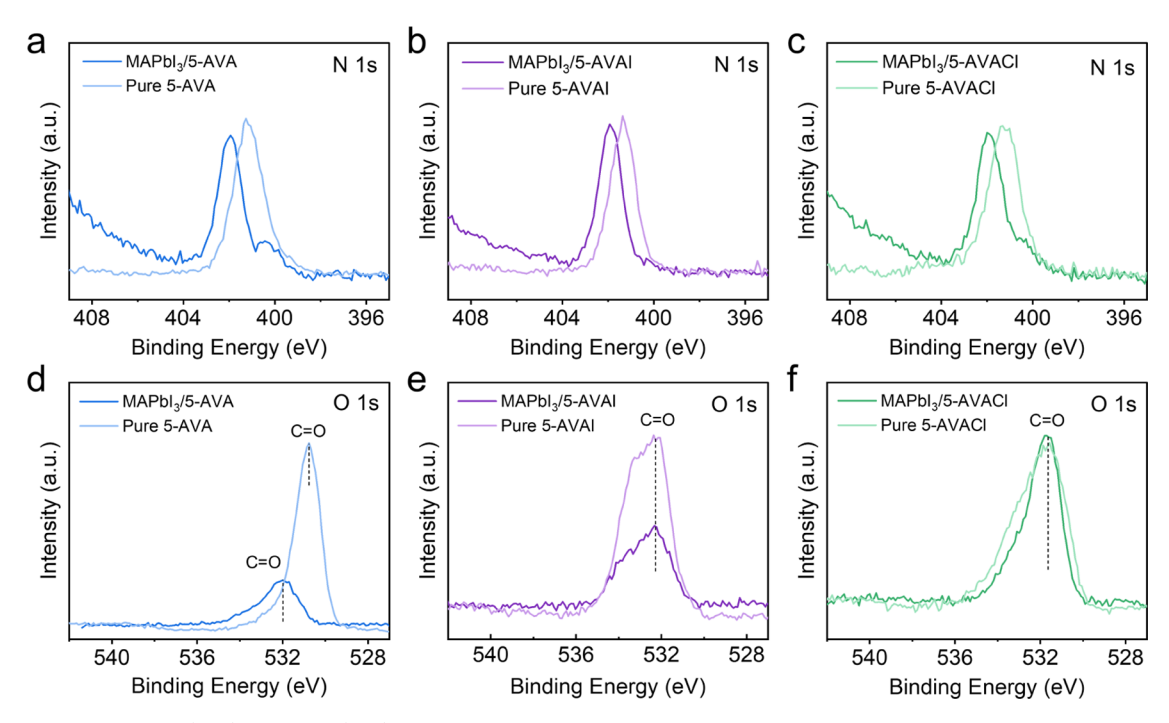


Figure 5. XPS spectra of the (a-c) N 1s and (d-f) O 1s signal of pure additives and MAPbI₃ films with 5-AVA, 5-AVAI, and 5-AVACl additives. An oxidative shift when the additives are added to films was observed in all N 1s spectra, indicating the nitrogens interacted with the MAPbI₃ surface. Conversely, an oxidative shift in the O 1s spectra was only observed with the 5-AVA additive, indicating that it was the only additive in which the C=O interacted with the MAPbI₃ surface.

of the geometrically optimized vacuum slab, and $E_{\rm additive}$ is the energy of the isolated adsorbate.

These results indicated that the preferential adsorption geometry of the 5-AVAX was independent of the halide species. That is, the most energetically favorable configuration for 5-AVAX was for the ammonium rather than the carboxyl functional group to be interacting with lead in the perovskite through $-NH_3^+ \cdots I^-$ or $X^- \cdots Pb^{2+}$ interactions (Figure 4a). Conversely, 5-AVA exhibited similar adsorption energies with both the amino and carboxyl functional groups interacting with the surface. Moreover, 5-AVAX species interacted more strongly with the perovskite surface (i.e., more negative adsorption energies) than 5-AVA because of the increased $X^{-} \cdots Pb^{2+}$ interaction strength over the $-N \cdots Pb^{2+}$ and $=O \cdots$ Pb²⁺ interactions in 5-AVA, along with stronger hydrogenbonding interactions with iodide species present on the perovskite surface, i.e., -NH₃+···I. Interestingly for 5-AVA, the strongest interaction was between the carboxyl group and the MA-I termination. Here, the carbonylic oxygen coordinated surface MA+ cations, while OH···I hydrogen bonding coordinated surface iodine (Figure 4b). For zwitterionic 5-AVA, we observed that -COO-...H hydrogen bonding and -COO-...Pb2+ coordination bonding dominate adsorption energy for MA-I and Pb-I surfaces terminations, respectively, which is consistent with the discussion of zwitterionic capping ligands by Kovalenko and co-workers. 60 We note that in the case of zwitterionic 5-AVA on the MA-I surface termination, no stable configuration was found for the isolated surface interaction of the ammonium functional group due to the strong electrostatic attraction between -COO and the mobile surface methylammonium cations.

Of particular interest was 5-AVACl, which exhibited different behavior than the other additives. With 5-AVACl, all energy-optimized adsorption geometries with the ammo-

nium halide functional group pointing away from the perovskite surface exhibited the dissociation of 5-AVACl into 5-AVA and HCl, where the chloride ion was protonated by the ammonium species (Figure S8). We further confirmed this observation by analyzing the electron localization function (ELF) of the 5-AVA/5-AVAX molecules and then looking at the 5-AVACl adsorption geometries on the MAPbI3 surface (Figure S9). From the DFT calculations, we predict that the dominant interactions between 5-AVA/decomposed 5-AVACl and perovskite could be $-N \cdot \cdot \cdot Pb^{2+}$ or $= O \cdot \cdot \cdot Pb^{2+}$ coordination bonding, while the interaction between 5-AVAI/intact 5-AVACl and perovskite could be X-...Pb2+ ionic bonding and -NH₃+···I[−] hydrogen bonding. We explored this behavior more thoroughly by performing DFT calculations of isolated molecules in vacuum and creating electrostatic potential maps for 5-AVAI and 5-AVACl (Figure 4c). Our calculations revealed an interesting deviation in behavior between the halogenated 5-AVAX species. During geometry optimization, the iodide in 5-AVAI remained coulombically bound to the ammonium group, while 5-AVACl dissociated into 5-AVA and HCl as previously described (Figure 4c). This degradation of 5-AVACl was attributed to the higher electronegativity of the chloride ion relative to the iodide ion, leading to a pronounced N/H-Cl bonding character. 47,61 Additionally, the formation of HCl by the dissociation of 5-AVACl is consistent with the decomposition of chloride-containing organic/inorganic metal halide perovskites, such as MAPbCl₃, which have been demonstrated to form gaseous methylamine and hydrogen chloride as decomposition products.⁶²

We also probed the possibility of halide exchange in the case of 5-AVACl addition by performing adsorption calculations with chloride ion incorporation within the top layer of each perovskite termination. Our calculations suggested that this halide exchange is energetically unfavorable, with a change of

ACS Applied Materials & Interfaces

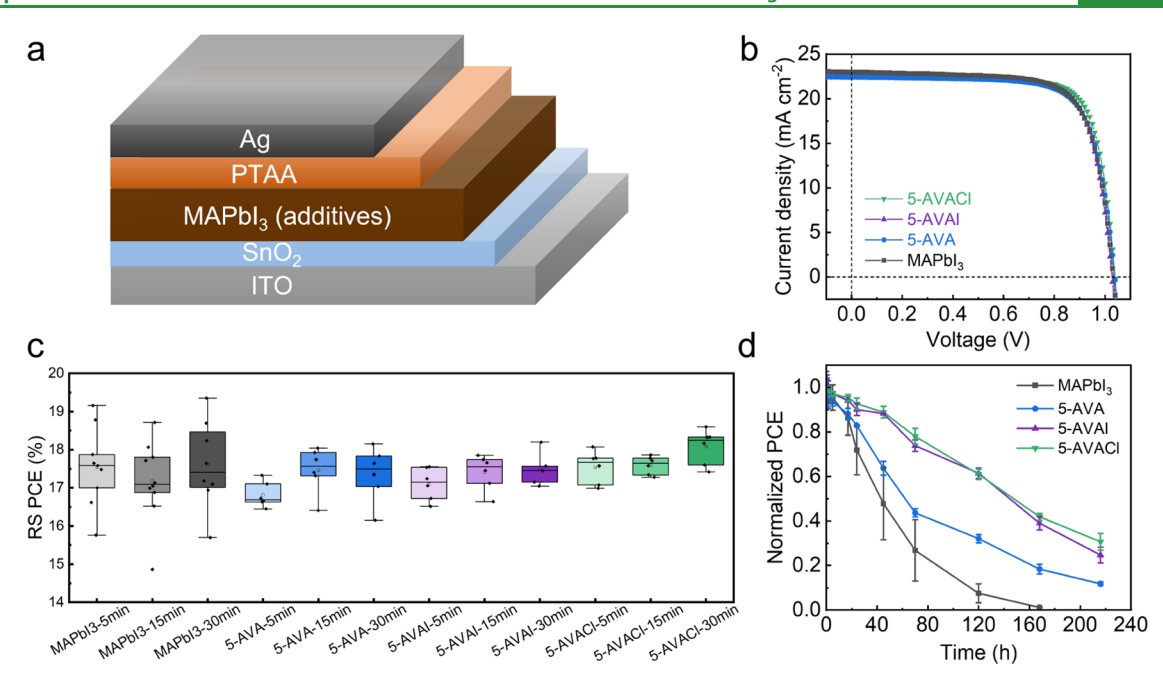


Figure 6. Solar cell characteristics of MAPbI $_3$ and additive devices. (a) Device configuration of the perovskite solar cell. (b) J-V curves of MAPbI $_3$ -based solar cells without and with additives. (c) Statistical distribution of PCE without and with additives at different annealing times. (d) Moisture stability of unencapsulated devices without and with additives under 50% RH at room temperature.

0.1315 and 0.0865 eV for the MA-I- and Pb-I-rich surfaces, respectively (Figure S10).

The interactions between 5-AVA/5-AVAX and the MAPbI₃ were further confirmed by XPS. The XPS results with 1 mol % additives incorporated in the bulk films are shown in Figure S11. However, the low concentration of the additives made it challenging to detect the additives' signals and determine their interactions with the perovskite. To enhance the interaction strength of perovskite with additives and amplify the signals, the films used for XPS measurement were prepared by spincoating 5-AVA/5-AVAX (0.01 mmol mL⁻¹ in anhydrous IPA) on top of pristine MAPbI3 films. As a control, pure IPA was spin-coated onto pristine MAPbI3 to account for any interactions between the IPA and perovskite. To determine which functional groups of the additives interacted more strongly with the perovskite surface, we compared the XPS binding energies for N 1s and O 1s of films with additives to the pure additives. In the N 1s spectra of the films, an oxidative shift was observed in all cases—0.7, 0.6, and 0.7 eV shift for 5-AVA, 5-AVAI, and 5-AVACl films, respectively—compared to the pure additives, suggesting that the amino/ammonium groups in all additives interacted with the perovskite surface. Conversely, binding energy shifts of O 1s peaks showed different behaviors in 5-AVA and 5-AVAX films. The binding energy of the C=O group in MAPbI₃ with 5-AVA was blueshifted to 531.9 eV compared to pure 5-AVA (530.8 eV), suggesting a coordination interaction of the C=O group with Pb²⁺. ⁴³ Conversely, in films with 5-AVAX additives, the C=O group binding energies were relatively unchanged compared to the pure additives, indicating fewer C=O···Pb²⁺ interactions in these films (Figure 5). These observations agreed with the DFT calculations of additive adsorption energy, indicating that while amino acids interacted with MAPbI3 surfaces through both functional groups, while ammonium acids exhibited strong preferential interactions through the ammonium groups.

A comparison of the C 1s, Pb 4f, N 1s, O 1s, I 3d, and Cl 2p XPS peaks for the control and 5-AVA/5-AVAX samples is

shown in Figure S12. The binding energy was calibrated by setting the aliphatic hydrocarbon C 1s peak to 284.8 eV. The C 1s peaks at 285.9–286.1 eV were assigned to the MA⁺ group in MAPbI₃. In all films with additives, there was an increased C= O signal in C 1s and O 1s spectra, indicating that the additives remained present in the films and were not volatilized. In pristine MAPbI₃, oxygen and some non-MA⁺ carbon were also detected because of the residual IPA and adventitious adsorbed carbon and oxygen. The Cl 2p signal confirmed that chloride was only present in the films with added 5-AVACl. The peaks of Pb $4f_{5/2}$ and Pb $4f_{7/2}$ in the pristine MAPbI₃ were at binding energies of 138.3 and 143.1 eV, but with the inclusion of the 5-AVA/5-AVAX additives, these peaks shifted to lower binding energies-138.2 and 143.0 eV in films with 5-AVA and 5-AVACl and 138.0 and 142.9 eV in films with 5-AVAI. In films with additives, the small shoulder peaks around 136.4 and 141.3 eV were assigned to metallic Pb. 63 The Pb0 impurities are likely decomposition byproducts of lead halides, often observed in the lead halide-rich perovskite films from posthigh-photon-energy measurement processes such as XPS. 63,64 The increased Pb⁰ peak in the films with additives indicated that these additives might accelerate the decomposition of Pb²⁺ to Pb⁰ under high-energy light. This observation was consistent with a previous study by Hu et al. that showed that amine- and ammonium-based additives can reduce Pb2+ to Pb0 if there is an accessible β -carbon hydrogen that can react with iodine in the perovskite to form HI.65

The Pb 4f peak was red-shifted in films with 5-AVA and 5-AVACl, which we attributed to C=O···Pb²⁺ or -N···Pb²⁺ coordination and Pb-Cl ionic bonding passivating the undercoordinated Pb²⁺. The further reduction observed in the Pb 4f binding energy in films with 5-AVAI suggested its interaction with Pb²⁺ was the strongest, which was consistent with the DFT calculations. Element quantification (Table S4) showed that the atomic concentration ratio of I/Pb in 5-AVAI film was about 3.24, which was larger than the I/Pb ratio of 3 in an ideal MAPbI₃, implying that there was an excess of iodine

Table 1. Power Conversion Efficiencies (PCEs) of ITO/SnO₂/MAPbI₃ (with or without 1 mol % Additive)/PTAA/Ag

perovskite composition	avg. PCE (%)	$V_{\rm oc}$ (V)	$J_{\rm sc}~({\rm mA~cm^{-2}})$	FF (%)
$MAPbI_3$	17.606 ± 1.071	1.034 ± 0.020	22.984 ± 0.503	74.03 ± 2.88
w/1 mol% 5-AVA	17.361 ± 0.645	1.038 ± 0.007	22.404 ± 0.308	74.65 ± 2.80
w/1 mol% 5-AVAI	17.481 ± 0.405	1.027 ± 0.007	22.535 ± 0.215	75.53 ± 1.17
w/1 mol% 5-AVACl	18.074 ± 0.422	1.039 ± 0.008	22.452 ± 0.172	77.47 ± 1.07

present on the surface. Given the surface sensitivity of XPS, it is likely that our deposition technique for these measurements-spin-coating of the additives on top of the film to amplify the signals—resulted in deviations of the I/Pb ratios in all films with additives; however, the inclusion of 5-AVAI was the only case that showed an increase in I/Pb ratio relative to the pristine MAPbI₃. This excess free I on the perovskite surface could form stronger Pb-I bonding compared to the C=O···Pb²⁺ or −N···Pb²⁺ coordination bonding in films with 5-AVA and 5-AVACl, resulting in further increased electron density and reduced oxidation of Pb2+. A slight red shift was also observed for I 3d peaks in films with 5-AVAI (630.5 and 619.0 eV), while films with 5-AVA and 5-AVACl samples showed identical binding energies of 630.6 and 619.1 eV with the control sample (Figure S12), which also provided evidence for the presence of excess I on the surface of the film with 5-AVAI.

The N 1s peaks at 401.9-402.1 eV were assigned to ammonium groups (-NH₃⁺) in MA⁺, 5-AVAX, or zwitterionic 5-AVA. 66 An additional peak was observed at 400.2-400.5 eV, which was assigned to amino groups (-NH₂); this amino group could be from either 5-AVA (or 5-AVACl that decomposed to 5-AVA) or CH3NH2 that has decomposed from MAI. 66,67 The increased -NH3+ and decreased -NH2 intensity and in the film with 5-AVAI indicated that the N atoms in 5-AVAI were mainly in a -NH₃⁺ form, while N in 5-AVA and 5-AVACl included significantly more -NH2, in agreement with the simulation predictions discussed above. Since the -NH3+ signal was a convolution of the methylammonium and ammonium groups in 5-AVAI and 5-AVACl, it was difficult to identify the peak shift only attributable to the additives to determine their interaction with perovskite. However, for the films with 5-AVAI and 5-AVACl, the -NH3+ peaks shifted toward lower binding energies compared to the pristine MAPbI3 film (with an FWHM of 1.14) with slightly broadened FWHMs of 1.16 and 1.19, so we speculated there were chemical interactions between the ammonium groups of the 5-AVAX and the iodide in the perovskite, likely through hydrogen bonding.²⁰

3.5. Device Performance and Stability. We fabricated solar cells with an n-i-p architecture (Figure 6a) to test the performance and stability of MAPbI₃ with the inclusion of 5-AVA/5-AVAX additives. The averaged current densityvoltage (J-V) curves of the MAPbI₃-based solar cells with and without 5-AVA/5-AVAX additives are shown in Figure 6b, and their corresponding statistics of the photovoltaic parameters, which were measured for a minimum of six devices of each type, are summarized in Figure 6c and Table 1. We observed that with the inclusion of additives, device performance was more repeatable—i.e., had a tighter distribution of PCEs—than with pristine devices (Figure 6b,c). PSCs with pristine MAPbI₃ had an average power conversion efficiency (PCE) of 17.606 ± 1.071%, with an open-circuit voltage (V_{oc}) of 1.034 \pm 0.020 V, a short-circuit current density (J_{sc}) of 22.984 \pm 0.503 mA cm⁻², and a fill

factor (FF) of 74.03 \pm 2.88%. The average PCEs for the devices incorporating 1 mol % 5-AVA (17.361 \pm 0.645%) and 5-AVAI (17.481 \pm 0.405%) were similar to pristine MAPbI₃ devices. For the devices with 1 mol % 5-AVACI, the average PCE increased to 18.074 \pm 0.422%, an ~4% efficiency improvement, which was mostly attributed to a significantly increased fill factor from 74.03 \pm 2.88 to 77.47 \pm 1.07% (Table 1). At concentrations of 5% and above, all three additives showed detrimental effects to PCE. The average PCEs dropped to 10.285 \pm 4.201, 12.921 \pm 1.476, and 15.026 \pm 0.319% for the devices incorporating 5 mol % 5-AVA, 5-AVAI, and 5-AVACI, respectively (Figure S13). This decrease in PCE induced by higher concentrations of additives was likely due to their insulating nature hindering interfacial charge transport.²⁵

Passivation of defects in perovskites has been shown to not only improve device performance but also improve device stability. We therefore tested the moisture stability of unencapsulated devices in air at 50% relative humidity and room temperature. The normalized PCE vs time is shown in Figure 6d, and the raw PCE values are reported in Table SS. All devices used in this experiment had been fabricated and then stored in a glovebox (nitrogen environment in the dark) for 15 days before beginning the stability tests. After 70 h of aging in a moist environment, the average PCE retention of the pristine MAPbI₃ devices was only 26.3 \pm 12.1%. With the inclusion of 5-AVA, after 70 h, 45.6 \pm 4.6% of the initial PCE was retained. Adding ammonium acids resulted in significantly improved stability, with 70 h PCE retention of 74.2 \pm 5.3% with 5-AVAI and 80.5 \pm 3.0% with 5-AVACI.

4. CONCLUSIONS

ı

In this work, we studied a series of amino and ammonium acids to show how halides influence the performance and stability of metal halide perovskite films and devices. The inclusion of 5-AVAI and 5-AVACl resulted in films with larger grain sizes, which we attributed to slower crystallization, and potential templating. With respect to device performance, the inclusion of additives resulted in greater reproducibility, and with the inclusion of 5-AVACl, noticeably improved average device efficiencies compared to devices comprising pristine perovskite. Furthermore, we observed improved stability to mild aging conditions (50% RH and 25 °C) by incorporating all additives, but with ammonium acid-based devices having significantly improved lifetimes.

This study is the first to introduce 5-AVACl into perovskite precursor solutions to synthesize 3D perovskite films, building on previous studies that had demonstrated the inclusion of 5-AVAI was beneficial for MAPbI₃ device efficiency and stability and others that had shown that chloride inclusion increases the size of perovskite grains.²⁸ We used DFT to show that this 5-AVACl additive acts similarly to 5-AVAI while in solution state, and to 5-AVA while in solid state after solvent evaporation due to the Cl⁻ reacting with hydrogen on the ammonium group to form HCl, which then results in Lewis

acid—base interactions between surface Pb^{2+} and the remaining NH_2 functional group. This observation of HCl evolution is likely translatable to other molecular additives incorporating ammonium chloride groups, such as methylammonium chloride, and could be a useful strategy for improving device efficiency, stability, and processing repeatability.

ASSOCIATED CONTENT

Supporting Information

The Supporting Information is available free of charge at https://pubs.acs.org/doi/10.1021/acsami.3c01432.

Additional XRD patterns and data; additional steady-state PL spectra; time-resolved PL fitting results; UV—vis absorption spectra; grain size distribution histograms; additional DFT calculations; adsorption geometries; DFT-calculated adsorption geometries for 5-AVAX and electron localization function analysis for 5-AVACl; XPS spectra and element quantification; J—V curves; and absolute PCE data (PDF)

AUTHOR INFORMATION

Corresponding Author

Adam D. Printz — Department of Chemical and Environmental Engineering and Department of Materials Science and Engineering, University of Arizona, Tucson, Arizona 85721, United States; Occid.org/0000-0002-5264-7792; Phone: +1 520 626 6769; Email: aprintz@arizona.edu

Authors

Yanan Li — Department of Chemical and Environmental Engineering, University of Arizona, Tucson, Arizona 85721, United States

Patrick J. Lohr – Department of Chemical and Environmental Engineering, University of Arizona, Tucson, Arizona 85721, United States

Allison Segapeli – Department of Chemical and Environmental Engineering, University of Arizona, Tucson, Arizona 85721, United States

Juliana Baltram – Department of Chemical and Environmental Engineering, University of Arizona, Tucson, Arizona 85721, United States

Dorian Werner – Department of Chemical and Environmental Engineering, University of Arizona, Tucson, Arizona 85721, United States

Alex Allred — Department of Chemical and Environmental Engineering, University of Arizona, Tucson, Arizona 85721, United States

Krishna Muralidharan — Department of Materials Science and Engineering, University of Arizona, Tucson, Arizona 85721, United States; orcid.org/0000-0003-1275-3846

Complete contact information is available at: https://pubs.acs.org/10.1021/acsami.3c01432

Author Contributions

 $\fint{Y.L.}$ and P.J.L. contributed equally to this work.

Notes

The authors declare no competing financial interest.

ACKNOWLEDGMENTS

This material is based upon work supported by the National Science Foundation under grant no. 2237211. This work was

further supported by laboratory startup funds from the University of Arizona. P.J.L. was supported by the financial and in-kind contributions of the University of Arizona University Fellows Program. The authors thank the following user facilities at the University of Arizona. All Park AFM images and data were collected in the W.M. Keck Center for Nano-Scale Imaging in the Department of Chemistry and Biochemistry at the University of Arizona, RRID:SCR 022884. This instrument purchase was partially supported by Arizona Technology and Research Initiative Fund (A.R.S.§15-1648). All X-ray and ultraviolet photoelectron spectra were collected at the Laboratory for Electron Spectroscopy and Surface Analysis (LESSA) in the Department of Chemistry and Biochemistry at the University of Arizona, RRID:SCR 022885, using a Kratos Axis 165 Ultra DLD Hybrid Ultrahigh Vacuum Photoelectron Spectrometer. The instrument was purchased with funding from the National Science Foundation and supported by the Center for Interface Science: Solar-Electric Materials (CIS:SEM), an Energy Frontier Research Center funded by the U.S. Department of Energy and Arizona Technology and Research Initiative Fund (A.R.S.§15-1648). The powder XRD measurements were performed at the XRD facility in the Department of Chemistry and Biochemistry of the University of Arizona, RRID:SCR 022886, on a Philips PANalytical X'Pert PRO MPD instrument. The authors acknowledge NASA grants #NNX12AL47G and #NNX15AJ22G and NSF grant #1531243 for funding of the instrumentation in the Kuiper Materials Imaging and Characterization Facility at the University of Arizona. UV-vis spectrometry was performed at the Micro/Nanofabrication Center at the University of Arizona. DFT calculations were performed upon High Performance Computing (HPC) resources supported by the University of Arizona TRIF, UITS, and Research, Innovation, and Impact (RII) and maintained by the University of Arizona Research Technologies Department.

REFERENCES

- (1) Noh, J. H.; Im, S. H.; Heo, J. H.; Mandal, T. N.; Seok, S. I. Chemical Management for Colorful, Efficient, and Stable Inorganic—Organic Hybrid Nanostructured Solar Cells. *Nano Lett.* **2013**, *13*, 1764–1769.
- (2) Stranks, S. D.; Eperon, G. E.; Grancini, G.; Menelaou, C.; Alcocer, M. J. P.; Leijtens, T.; Herz, L. M.; Petrozza, A.; Snaith, H. J. Electron-Hole Diffusion Lengths Exceeding 1 Micrometer in an Organometal Trihalide Perovskite Absorber. *Science* **2013**, 342, 341–344
- (3) Dong, Q.; Fang, Y.; Shao, Y.; Mulligan, P.; Qiu, J.; Cao, L.; Huang, J. Electron-Hole Diffusion Lengths > 175 Mm in Solution-Grown CH 3 NH 3 PbI 3 Single Crystals. *Science* **2015**, 347, 967–970
- (4) Li, Y.; Dailey, M.; Lohr, P. J.; Printz, A. D. Performance and Stability Improvements in Metal Halide Perovskite with Intralayer Incorporation of Organic Additives. *J. Mater. Chem. A* **2021**, *9*, 16281–16338.
- (5) National Renewable Energy Laboratory. Best Research-Cell Efficiencies, 2020.
- (6) Yoo, J. J.; Seo, G.; Chua, M. R.; Park, T. G.; Lu, Y.; Rotermund, F.; Kim, Y.; Moon, C. S.; Jeon, N. J.; Correa-Baena, J.-P.; Bulović, V.; Shin, S. S.; Bawendi, M. G.; Seo, J. Efficient Perovskite Solar Cells via Improved Carrier Management. *Nature* **2021**, *590*, 587–593.
- (7) Jeong, J.; Kim, M.; Seo, J.; Lu, H.; Ahlawat, P.; Mishra, A.; Yang, Y.; Hope, M. A.; Eickemeyer, F. T.; Kim, M.; Yoon, Y. J.; Choi, I. W.; Darwich, B. P.; Choi, S. J.; Jo, Y.; Lee, J. H.; Walker, B.; Zakeeruddin, S. M.; Emsley, L.; Rothlisberger, U.; Hagfeldt, A.; Kim, D. S.; Grätzel,

- M.; Kim, J. Y. Pseudo-Halide Anion Engineering for α -FAPbI3 Perovskite Solar Cells. *Nature* **2021**, *592*, 381–385.
- (8) Rolston, N.; Printz, A. D.; Tracy, J. M.; Weerasinghe, H. C.; Vak, D.; Haur, L. J.; Priyadarshi, A.; Mathews, N.; Slotcavage, D. J.; McGehee, M. D.; Kalan, R. E.; Zielinski, K.; Grimm, R. L.; Tsai, H.; Nie, W.; Mohite, A. D.; Gholipour, S.; Saliba, M.; Grätzel, M.; Dauskardt, R. H. Effect of Cation Composition on the Mechanical Stability of Perovskite Solar Cells. *Adv. Energy Mater.* **2018**, 8, No. 1702116.
- (9) Zhou, Y.; Zhao, Y. Chemical Stability and Instability of Inorganic Halide Perovskites. *Energy Environ. Sci.* **2019**, *12*, 1495–1511.
- (10) Ding, D.; Li, H.; Li, J.; Li, Z.; Yao, H.; Liu, L.; Tian, B. B.; Su, C.; Chen, F.; Shi, Y. Effect of Mechanical Forces on Thermal Stability Reinforcement for Lead Based Perovskite Materials. *J. Mater. Chem. A* **2019**, *7*, 540–548.
- (11) Fu, Y.; Wu, T.; Wang, J.; Zhai, J.; Shearer, M. J.; Zhao, Y.; Hamers, R. J.; Kan, E.; Deng, K.; Zhu, X.-Y.; Jin, S. Stabilization of the Metastable Lead Iodide Perovskite Phase via Surface Functionalization. *Nano Lett.* **2017**, *17*, 4405–4414.
- (12) Feng, W.; Zhang, C.; Zhong, J.-X.; Ding, L.; Wu, W.-Q. Correlating Alkyl Chain Length with Defect Passivation Efficacy in Perovskite Solar Cells. *Chem. Commun.* **2020**, *56*, 5006–5009.
- (13) Gutwald, M.; Rolston, N.; Printz, A. D.; Zhao, O.; Elmaraghi, H.; Ding, Y.; Zhang, J.; Dauskardt, R. H. Perspectives on Intrinsic Toughening Strategies and Passivation of Perovskite Films with Organic Additives. *Sol. Energy Mater. Sol. Cells* **2020**, 209, No. 110433.
- (14) Wu, W.-Q.; Yang, Z.; Rudd, P. N.; Shao, Y.; Dai, X.; Wei, H.; Zhao, J.; Fang, Y.; Wang, Q.; Liu, Y.; Deng, Y.; Xiao, X.; Feng, Y.; Huang, J. Bilateral Alkylamine for Suppressing Charge Recombination and Improving Stability in Blade-Coated Perovskite Solar Cells. *Sci. Adv.* 2019, *5*, No. eaav8925.
- (15) Park, S. M.; Abtahi, A.; Boehm, A. M.; Graham, K. R. Surface Ligands for Methylammonium Lead Iodide Films: Surface Coverage, Energetics, and Photovoltaic Performance. *ACS Energy Lett.* **2020**, *5*, 799–806.
- (16) Zheng, X.; Chen, B.; Dai, J.; Fang, Y.; Bai, Y.; Lin, Y.; Wei, H.; Zeng, X. C.; Huang, J. Defect Passivation in Hybrid Perovskite Solar Cells Using Quaternary Ammonium Halide Anions and Cations. *Nat. Energy* **2017**, *2*, No. 17102.
- (17) Lu, J.; Jiang, L.; Li, W.; Li, F.; Pai, N. K.; Scully, A. D.; Tsai, C.-M.; Bach, U.; Simonov, A. N.; Cheng, Y.-B.; Spiccia, L. Diammonium and Monoammonium Mixed-Organic-Cation Perovskites for High Performance Solar Cells with Improved Stability. *Adv. Energy Mater.* 2017, 7, No. 1700444.
- (18) Mei, A.; Li, X.; Liu, L.; Ku, Z.; Liu, T.; Rong, Y.; Xu, M.; Hu, M.; Chen, J.; Yang, Y.; Gratzel, M.; Han, H. A Hole-Conductor-Free, Fully Printable Mesoscopic Perovskite Solar Cell with High Stability. *Science* **2014**, *345*, 295–298.
- (19) Grancini, G.; Roldán-Carmona, C.; Zimmermann, I.; Mosconi, E.; Lee, X.; Martineau, D.; Narbey, S.; Oswald, F.; De Angelis, F.; Graetzel, M.; Nazeeruddin, M. K. One-Year Stable Perovskite Solar Cells by 2D/3D Interface Engineering. *Nat. Commun.* **2017**, 8, No. 15684.
- (20) Alanazi, A. Q.; Kubicki, D. J.; Prochowicz, D.; Alharbi, E. A.; Bouduban, M. E. F.; Jahanbakhshi, F.; Mladenović, M.; Milić, J. V.; Giordano, F.; Ren, D.; Alyamani, A. Y.; Albrithen, H.; Albadri, A.; Alotaibi, M. H.; Moser, J.-E.; Zakeeruddin, S. M.; Rothlisberger, U.; Emsley, L.; Grätzel, M. Atomic-Level Microstructure of Efficient Formamidinium-Based Perovskite Solar Cells Stabilized by 5-Ammonium Valeric Acid Iodide Revealed by Multinuclear and Two-Dimensional Solid-State NMR. J. Am. Chem. Soc. 2019, 141, 17659–17669.
- (21) Kayesh, M. E.; Matsuishi, K.; Kaneko, R.; Kazaoui, S.; Lee, J.; Noda, T.; Islam, A. Coadditive Engineering with 5-Ammonium Valeric Acid Iodide for Efficient and Stable Sn Perovskite Solar Cells. *ACS Energy Lett.* **2019**, *4*, 278–284.
- (22) Shi, Y.; Hu, J.; Chen, J.; Xu, Y.; Yang, W.; Chen, J.; He, Y. S-Ammoniumvaleric Acid Stabilized Mixed-Dimensional Perovskite

- Submicron Platelets with White Light Emission. *Nanoscale Adv.* **2020**, *2*, 4822–4829.
- (23) Kim, M.; Figueroa-Tapia, J. M.; Prato, M.; Petrozza, A. Engineering Multiphase Metal Halide Perovskites Thin Films for Stable and Efficient Solar Cells. *Adv. Energy Mater.* **2020**, *10*, No. 1903221.
- (24) Mei, A.; Sheng, Y.; Ming, Y.; Hu, Y.; Rong, Y.; Zhang, W.; Luo, S.; Na, G.; Tian, C.; Hou, X.; Xiong, Y.; Zhang, Z.; Liu, S.; Uchida, S.; Kim, T. W.; Yuan, Y.; Zhang, L.; Zhou, Y.; Han, H. Stabilizing Perovskite Solar Cells to IEC61215:2016 Standards with over 9,000-h Operational Tracking. *Joule* 2020, 4, 2646—2660.
- (25) Chen, J.; Seo, J. Y.; Park, N. G. Simultaneous Improvement of Photovoltaic Performance and Stability by In Situ Formation of 2D Perovskite at (FAPbI3)0.88(CsPbBr3)0.12/CuSCN Interface. *Adv. Energy Mater.* **2018**, 8, No. 1702714.
- (26) Zhao, Y.; Zhu, K. CH 3 NH 3 Cl-Assisted One-Step Solution Growth of CH 3 NH 3 PbI 3: Structure, Charge-Carrier Dynamics, and Photovoltaic Properties of Perovskite Solar Cells. *J. Phys. Chem. C* **2014**, *118*, 9412–9418.
- (27) Chen, B.; Yu, Z.; Liu, K.; Zheng, X.; Liu, Y.; Shi, J.; Spronk, D.; Rudd, P. N.; Holman, Z.; Huang, J. Grain Engineering for Perovskite/Silicon Monolithic Tandem Solar Cells with Efficiency of 25.4%. *Joule* **2019**, *3*, 177–190.
- (28) Li, M.; Li, B.; Cao, G.; Tian, J. Monolithic MAPbI3 Films for High-Efficiency Solar Cells: Via Coordination and a Heat Assisted Process. J. Mater. Chem. A 2017, 5, 21313–21319.
- (29) Ono, L. K.; Juarez-Perez, E. J.; Qi, Y. Progress on Perovskite Materials and Solar Cells with Mixed Cations and Halide Anions. *ACS Appl. Mater. Interfaces* **2017**, *9*, 30197–30246.
- (30) Kim, M.; Kim, G.-H.; Lee, T. K.; Choi, I. W.; Choi, H. W.; Jo, Y.; Yoon, Y. J.; Kim, J. W.; Lee, J.; Huh, D.; Lee, H.; Kwak, S. K.; Kim, J. Y.; Kim, D. S. Methylammonium Chloride Induces Intermediate Phase Stabilization for Efficient Perovskite Solar Cells. *Joule* **2019**, *3*, 2179–2192.
- (31) Cheng, F.; Zhang, J.; Pauporté, T. Chlorides, Other Halides, and Pseudo-Halides as Additives for the Fabrication of Efficient and Stable Perovskite Solar Cells. *ChemSusChem* **2021**, *14*, 3665–3692.
- (32) Perdew, J. P.; Burke, K.; Ernzerhof, M. Generalized Gradient Approximation Made Simple. *Phys. Rev. Lett.* **1996**, *77*, 3865–3868.
- (33) Grimme, S.; Antony, J.; Ehrlich, S.; Krieg, H. A Consistent and Accurate Ab Initio Parametrization of Density Functional Dispersion Correction (DFT-D) for the 94 Elements H-Pu. *J. Chem. Phys.* **2010**, 132, No. 154104.
- (34) Kresse, G.; Hafner, J. Ab Initio Molecular Dynamics for Liquid Metals. *Phys. Rev. B* **1993**, *47*, 558–561.
- (35) Kresse, G.; Furthmüller, J. Efficiency of Ab-Initio Total Energy Calculations for Metals and Semiconductors Using a Plane-Wave Basis Set. *Comput. Mater. Sci.* **1996**, *6*, 15–50.
- (36) Kresse, G.; Furthmüller, J. Efficient Iterative Schemes for Ab Initio Total-Energy Calculations Using a Plane-Wave Basis Set. *Phys. Rev. B* **1996**, *54*, 11169–11186.
- (37) Kresse, G.; Joubert, D. From Ultrasoft Pseudopotentials to the Projector Augmented-Wave Method. *Phys. Rev. B* **1999**, *59*, 1758–1775
- (38) Monkhorst, H. J.; Pack, J. D. Special Points for Brillouin-Zone Integrations. *Phys. Rev. B* **1976**, *13*, 5188–5192.
- (39) Momma, K.; Izumi, F. VESTA 3 for Three-Dimensional Visualization of Crystal, Volumetric and Morphology Data. *J. Appl. Crystallogr.* **2011**, *44*, 1272–1276.
- (40) Chai, J.-D.; Head-Gordon, M. Long-Range Corrected Hybrid Density Functionals with Damped Atom—Atom Dispersion Corrections. *Phys. Chem. Chem. Phys.* **2008**, *10*, 6615—6620.
- (41) Weigend, F. Accurate Coulomb-Fitting Basis Sets for H to Rn. *Phys. Chem. Chem. Phys.* **2006**, *8*, 1057–1065.
- (42) Ye, T.; Bruno, A.; Han, G.; Koh, T. M.; Li, J.; Jamaludin, N. F.; Soci, C.; Mhaisalkar, S. G.; Leong, W. L. Efficient and Ambient-Air-Stable Solar Cell with Highly Oriented 2D@3D Perovskites. *Adv. Funct. Mater.* **2018**, 28, No. 1801654.

- (43) Zhu, L.; Cao, H.; Xue, C.; Zhang, H.; Qin, M.; Wang, J.; Wen, K.; Fu, Z.; Jiang, T.; Xu, L.; Zhang, Y.; Cao, Y.; Tu, C.; Zhang, J.; Liu, D.; Zhang, G.; Kong, D.; Fan, N.; Li, G.; Yi, C.; Peng, Q.; Chang, J.; Lu, X.; Wang, N.; Huang, W.; Wang, J. Unveiling the Additive-Assisted Oriented Growth of Perovskite Crystallite for High Performance Light-Emitting Diodes. *Nat. Commun.* 2021, 12, No. 5081.
- (44) Zhu, W.; Kang, L.; Yu, T.; Lv, B.; Wang, Y.; Chen, X.; Wang, X.; Zhou, Y.; Zou, Z. Facile Face-Down Annealing Triggered Remarkable Texture Development in CH3NH3PbI3 Films for High-Performance Perovskite Solar Cells. ACS Appl. Mater. Interfaces 2017, 9, 6104–6113.
- (45) Yun, S.-C.; Ma, S.; Kwon, H.-C.; Kim, K.; Jang, G.; Yang, H.; Moon, J. Amino Acid Salt-Driven Planar Hybrid Perovskite Solar Cells with Enhanced Humidity Stability. *Nano Energy* **2019**, *59*, 481–401
- (46) Ashari-Astani, N.; Jahanbakhshi, F.; Mladenović, M.; Alanazi, A. Q. M.; Ahmadabadi, I.; Ejtehadi, M. R.; Dar, M. I.; Grätzel, M.; Rothlisberger, U. Ruddlesden—Popper Phases of Methylammonium-Based Two-Dimensional Perovskites with 5-Ammonium Valeric Acid AVA2MAn—1PbnI3n+1 with n = 1, 2, and 3. *J. Phys. Chem. Lett.* **2019**, *10*, 3543—3549.
- (47) Krummer, M.; Zimmermann, B.; Klingenberg, P.; Daub, M.; Hillebrecht, H. Perovskite-Related 2D Compounds in the System 5-Amino Valerian Acid Cation/MA/Pb/X (X = Cl, Br) Synthesis, Crystal Structures, and Optical Properties. *Eur. J. Inorg. Chem.* **2020**, 2020, 4581–4592.
- (48) Mao, L.; Ke, W.; Pedesseau, L.; Wu, Y.; Katan, C.; Even, J.; Wasielewski, M. R.; Stoumpos, C. C.; Kanatzidis, M. G. Hybrid Dion–Jacobson 2D Lead Iodide Perovskites. *J. Am. Chem. Soc.* **2018**, 140, 3775–3783.
- (49) Droseros, N.; Longo, G.; Brauer, J. C.; Sessolo, M.; Bolink, H. J.; Banerji, N. Origin of the Enhanced Photoluminescence Quantum Yield in MAPbBr3 Perovskite with Reduced Crystal Size. *ACS Energy Lett.* **2018**, *3*, 1458–1466.
- (50) Harrington, G. F.; Santiso, J. Back-to-Basics Tutorial: X-Ray Diffraction of Thin Films. *J. Electroceram.* **2021**, *47*, 141–163.
- (51) van Franeker, J. J.; Hendriks, K. H.; Bruijnaers, B. J.; Verhoeven, M. W. G. M.; Wienk, M. M.; Janssen, R. A. J. Monitoring Thermal Annealing of Perovskite Solar Cells with In Situ Photoluminescence. *Adv. Energy Mater.* **2017**, *7*, No. 1601822.
- (52) Yang, S.; Dai, J.; Yu, Z.; Shao, Y.; Zhou, Y.; Xiao, X.; Zeng, X. C.; Huang, J. Tailoring Passivation Molecular Structures for Extremely Small Open-Circuit Voltage Loss in Perovskite Solar Cells. J. Am. Chem. Soc. 2019, 141, 5781–5787.
- (53) Ambrosio, F.; Mosconi, E.; Alasmari, A. A.; Alasmary, F. A. S.; Meggiolaro, D.; De Angelis, F. Formation of Color Centers in Lead Iodide Perovskites: Self-Trapping and Defects in the Bulk and Surfaces. *Chem. Mater.* **2020**, *32*, 6916–6924.
- (54) Yang, B.; Keum, J.; Ovchinnikova, O. S.; Belianinov, A.; Chen, S.; Du, M.-H.; Ivanov, I. N.; Rouleau, C. M.; Geohegan, D. B.; Xiao, K. Deciphering Halogen Competition in Organometallic Halide Perovskite Growth. *J. Am. Chem. Soc.* **2016**, *138*, 5028–5035.
- (55) Tantardini, C.; Kokott, S.; Gonze, X.; Levchenko, S. V.; Saidi, W. A. "Self-Trapping" in Solar Cell Hybrid Inorganic-Organic Perovskite Absorbers. *Appl. Mater. Today* **2022**, *26*, No. 101380.
- (56) Das, T.; Di Liberto, G.; Pacchioni, G. Density Functional Theory Estimate of Halide Perovskite Band Gap: When Spin Orbit Coupling Helps. *J. Phys. Chem. C* **2022**, *126*, 2184–2198.
- (57) Lin, C.-T.; Xu, W.; Macdonald, T. J.; et al. Correlating the Active Layer Structure and Composition with the Device Performance and Lifetime of Amino-Acid-Modified Perovskite Solar Cells. ACS Appl. Mater. Interfaces 2021, 13 (36), 43505–43515.
- (58) Wang, Q.; Chen, B.; Liu, Y.; Deng, Y.; Bai, Y.; Dong, Q.; Huang, J. Scaling Behavior of Moisture-Induced Grain Degradation in Polycrystalline Hybrid Perovskite Thin Films. *Energy Environ. Sci.* **2017**, *10*, 516–522.
- (59) She, L.; Liu, M.; Zhong, D. Atomic Structures of CH3NH3PbI3 (001) Surfaces. ACS Nano 2016, 10, 1126-1131.

- (60) Krieg, F.; Ochsenbein, S. T.; Yakunin, S.; ten Brinck, S.; Aellen, P.; Süess, A.; Clerc, B.; Guggisberg, D.; Nazarenko, O.; Shynkarenko, Y.; Kumar, S.; Shih, C.-J.; Infante, I.; Kovalenko, M. V. Colloidal CsPbX3 (X = Cl, Br, I) Nanocrystals 2.0: Zwitterionic Capping Ligands for Improved Durability and Stability. *ACS Energy Lett.* **2018**, 3, 641–646.
- (61) Chenon, B.; Sandorfy, C. Hydrogen Bonding in the Amine Hydrohalides: I. General Aspects. *Can. J. Chem.* **1958**, *36*, 1181–1206.
- (62) Brunetti, B.; Cavallo, C.; Ciccioli, A.; Gigli, G.; Latini, A. On the Thermal and Thermodynamic (In)Stability of Methylammonium Lead Halide Perovskites. *Sci. Rep.* **2016**, *6*, No. 31896.
- (63) Wincukiewicz, A.; Jasinski, J. B.; Tokarczyk, M.; Pietruszka, R.; Godlewski, M.; Kaminska, M. The Effects of Doping and Coating on Degradation Kinetics in Perovskites. *Sol. Energy Mater. Sol. Cells* **2021**, 230, No. 111142.
- (64) Liang, J.; Hu, X.; Yu, R.; Ke, W.; Liang, J.; Hu, X.; Wang, C.; Liang, C.; Chen, C.; Xiao, M.; Li, J. Article Origins and Influences of Metallic Lead in Perovskite Solar Cells Origins and Influences. *Joule* **2022**, *6*, 816–833.
- (65) Hu, J.; Kerner, R. A.; Pelczer, I.; Rand, B. P.; Schwartz, J. Organoammonium-Ion-Based Perovskites Can Degrade to Pb 0 via Amine—Pb(II) Coordination. ACS Energy Lett. 2021, 6, 2262—2267.
- (66) Artemenko, A.; Shchukarev, A.; Štenclová, P.; Wågberg, T.; Segervald, J.; Jia, X.; Kromka, A. Reference XPS Spectra of Amino Acids. *IOP Conf. Ser.: Mater. Sci. Eng.* **2021**, *1050*, No. 12001.
- (67) Ke, C. R.; Lewis, D. J.; Walton, A. S.; Chen, Q.; Spencer, B. F.; Mokhtar, M. Z.; Compean-Gonzalez, C. L.; O'Brien, P.; Thomas, A. G.; Flavell, W. R. Air-Stable Methylammonium Lead Iodide Perovskite Thin Films Fabricated via Aerosol-Assisted Chemical Vapor Deposition from a Pseudohalide Pb(SCN)2 Precursor. ACS Appl. Energy Mater. 2019, 2, 6012–6022.
- (68) Jiang, Q.; Zhao, Y.; Zhang, X.; Yang, X.; Chen, Y.; Chu, Z.; Ye, Q.; Li, X.; Yin, Z.; You, J. Surface Passivation of Perovskite Film for Efficient Solar Cells. *Nat. Photonics* **2019**, *13*, 460–466.
- (69) Ahn, N.; Son, D. Y.; Jang, I. H.; Kang, S. M.; Choi, M.; Park, N. G. Highly Reproducible Perovskite Solar Cells with Average Efficiency of 18.3% and Best Efficiency of 19.7% Fabricated via Lewis Base Adduct of Lead(II) Iodide. J. Am. Chem. Soc. 2015, 137, 8696–8699.
- (70) Zhang, H.; Cheng, J.; Li, D.; Lin, F.; Mao, J.; Liang, C.; Jen, A. K. Y.; Grätzel, M.; Choy, W. C. H. Toward All Room-Temperature, Solution-Processed, High-Performance Planar Perovskite Solar Cells: A New Scheme of Pyridine-Promoted Perovskite Formation. *Adv. Mater.* **2017**, *29*, No. 1604695.